The Journal of Chemical Physics

Tailored energy level alignment at MoO_X/GaP interface for solar-driven redox flow battery application

Dowon Bae,[a*‡] Gerasimos Kanellos,[a‡] Kristina Wedege,[b] Emil Dražević,[b] Anders Bentien,[b] Wilson A. Smith[a*‖]

[a]Delft University of Technology, Department of Chemical Engineering - Materials for Energy Conversion and Storage (MECS), Delft 2629HZ, The Netherlands
[b]Department of Engineering – Aarhus University, Hangøvej 2, DK-8200 Aarhus,
Corresponding author – d.bae@tudelft.nl; w.smith@tudelft.nl
[‖]Current affiliation: Renewable & Sustainable Energy Institute, University of Colorado Boulder

ABSTRACT

MoO_X is commonly considered to be a high work-function semiconductor. From X-ray photoelectron spectroscopy and photo-electrochemical analysis, it is shown that MoO_X can be considered as an effective hole-transfer layer (HTL) for the GaP-based device. Specifically, in the absence of carbon contamination using an ion-beam cleaning step, the oxygen vacancy derived defect band located inside the band-gap becomes the main charge transfer mechanism. We demonstrate, for the first time, a device with a MoO_X/GaP junction that functions as an unbiased photo-charging cell for the redox flow battery system with $AQS/AQSH_2 \| I^-/I_3^-$ redox couples. This work has important implications toward enabling MoO_X applications beyond the conventional solar cells, including electrochemical energy storage and chemical conversion systems.

INTRODUCTION

Efficient charge carrier separation and transfer at the interface is a key parameter for high efficiency photovoltaic (PV) and photoelectrochemical (PEC) devices. In the case of the homogenous pn-junction device, this is enabled through dopant atoms, introduced in each surface region of the semiconductor, that creates a highly selective charge carrier mobility for holes and electrons, respectively. Alternatively, charge separation can be obtained by thin-film materials other than the absorber semiconductor (*i.e.*, heterogeneous). Crystalline silicon (c-Si) device with a wide band-gap a-Si:H layer represent a recent highly efficient PV cell architecture.[1] Similarly, the c-Si device with highly doped nanocrystalline Si (hydrogen treated nc-Si) layers have demonstrated a long-term stable PEC hydrogen production (*i.e.*, hydrogen evolution reaction – HER).[2] On the other hand, heterogeneous junction with various metal oxides provides an efficient charge carrier transfer.[3–6] This type of contact comes with a less parasitic optical loss which has been observed in the case of thin-film silicon contacts.[7,8] Furthermore, relatively lower process temperature for forming the metal oxide can minimize the possible thermal damage of the device.

Among the transition metal oxides, high work-function materials can provide good hole-selective transport when they form hetero-contacts with the photo-absorber. The difference between work functions of the metal oxides and Fermi level of the photo-absorber leads to a large energy band bending that allows only one type of carrier to pass through at the interface.[9] Some metal oxides with high work functions, such as MoO_X,[4,10] VO_X,[3,11] and NiO_X[12] has proven beneficial in hole-selective transfer layer (HTL). In recent years, remarkable achievements have been reported on the photo-devices using molybdenum oxide (MoO_X). MoO_X is a wide band-gap (3.0~3.3 eV) semiconductor, and its high work-function over 6 eV makes this material attractive as the HTL.[9,10] Including the monumental work by Battaglia et al.,[5] a number of efforts have been devoted to the development of efficient c-Si solar cells with MoO_X.[4–6,13] Wang[4] and Tong[13] applied a passivation interlayer for c-Si followed by MoO_X HTL deposition, while Bullock[10] and Battaglia[5] demonstrated directed hole transfer using a MoO_X/c-Si configuration.

Under light irradiance, the generated charge carriers will flow towards the path of least resistance, opting for a decrease in their free energy. The energy level alignment is, therefore, the primary parameter, contributing to efficient charge separation and reduced interface recombination. The MoO_X has sub-stoichiometric phases which inherently form a mid-gap state close to the conduction band (CB). In many cases, MoO_X has been studied as an HTL based on its induced mid-gap state. In particular, the focus has been on the process parameters effects, such as thickness, composition and temperature to find the optimal conditions to acquire high conversion efficiency.

Strangely, MoO_X has not yet been employed in conjunction with wide band-gap materials as an HTL. In the present study, we demonstrate the influence of deposition parameters of MoO_X on the band alignment with wide band-gap GaP and electrical behaviour. The GaP is also a good candidate for top-cell of the multi-junction device in space applications because of its high-temperature stability.[14] Owing to its potential for high photovoltage, the GaP also has been applied to PEC water splitting applications.[15,16] The present work, therefore, aims to provide the enhanced charge carrier pathway at the interface of a GaP-based device through an investigation on the physical and optical properties of sputtered MoO_X with various O_2/Ar ratio. Specifically, we have evaluated the effectiveness of a MoO_X HTL, combined with a GaP-based PEC device and Pt conducting catalyst, for photo-charging of the solar-rechargeable redox flow battery (RFB) cell containing the negative (I_3^-/I^-) and positive ($AQS/AQSH_2$) electrolytes.

The architectural concept of the solar-rechargeable RFB is an integration or combination of an RFB and a PEC or PV-assisted photo-charging cell. Recently, various efforts have been put into this field[17–20] in the wake of the maturation of PEC materials enabling its practical electrochemical energy storage applications. Wenjie et al.[17] reported a remarkable solar-to-chemical (STC) efficiency of 14.1% using a triple-junction III-V device. We emphasize that the PEC experiments in this study have been conducted using a single-junction GaP-based device so that we can focus on parameters merit the most attention for efficient carrier transfer at the MoO_X/GaP interface.

EXPERIMENTAL

Materials and fabrication process

For MoO_X thin films, Mo was sputtered on bare fluorine-doped tin oxide (FTO) coated glass substrate (TEC-15, Hartford glass co.), and n-type GaP wafers (300 µm, S-doped, [100]; ITME) in an argon background with various oxygen mixture ratio. Prior to the deposition samples were sputter-cleaned by Ar flow at 20 W for 3 minutes to remove contaminations and native oxide layers. To avoid contamination from the packaging material, all glass substrates were cleaned using an ultrasonic bath with DI water, ethanol and acetone for 20 minutes each. This was followed by N_2 gas drying before use. The total pressure during deposition was kept constant at 0.3 Pa and samples were prepared using different O_2 flows. The DC sputtering power was kept constant at 80 W, and all the samples were deposited at room temperature. The O_2/Ar ratios used for the preparation of the MoO_X thin films were 6/14, 7/13 and 8/12 standard cubic centimeters per minute (sccm). Analysis of the MoO_X film prepared at 5/15 O_2/Ar ratio was ruled out as it showed metal-like strong absorption in the visible region (Fig. S1), attributed to the excessive metal elements. The SiO_X and Mo interlayers at the interface were deposited using Si (99.999%) and Mo (99.95%) targets (from AJA international) at the same sputter system used for the MoO_X formation. The sputter gun-shutter was opened after a delay time expires (2 minutes after reaching the required power rate) to secure a stabilized chamber condition and deposition rate. In the case of the SiO_X, the Si target was sputtered under O_2 and Ar mixed gas flow (14:6). For each combination of DC sputtering parameters, two samples were prepared, one to be analyzed as-deposited and the other to be treated with post-deposition annealing in a furnace (Applied Test Systems, Inc.). It should be noted that the annealing temperature of 200˚C was chosen because intermediate band absorption has been observed for higher annealing temperatures.[21] In the case of PEC experiments, the GaP surface is coated with 10 nm Pt conducting film sputtered using the same procedure described elsewhere.[20,22]

Photoelectrode and flow cell

The photocathodes were prepared as described elsewhere and used without further optimization.[22,23] Briefly, Cu-wire is directly connected to the ring-shaped Au current-collector layer deposited on the light-illuminated side of the GaP photoelectrodes. The ring-shaped Au layer yields an active area of approximately 0.2 cm^2. In the two-electrode configuration, redox solutions, separated by a Nafion membrane, were circulated by a peristaltic pump at 70 mL min^{-1}. For redox couples, NaI and AQS (Anthraquinone-2-sulfonate) were used as anolyte and catholyte, respectively. The NaI (Sigma, ≥99.5%) was used were as received, and the AQS was prepared as described elsewhere.[24] As a counter electrode (*i.e.*, the anode in this case), a carbon felt formed on a carbon paper was used for both PEC and electrochemical experiments in the dark. For the flow battery test, electrolytes were pumped in through the neoprene tubing with a peristaltic pump (70 mL min^{-1}), and the cycling tests were conducted at room temperature with constant current charging and discharging using a commercial flow battery

cell with 25 cm^2 active area. It is worth noting that the solutions were purged with nitrogen before and during measurements.

Characterization and calculation

The optical properties of the MoO_X thin films were tested by UV-Vis spectroscopy using a Perkin-Elmer Lambda 900, and their thickness was determined by an interferometric surface profiler (Dektak 3) to determine band-gap. The structural properties of the films were examined using X-ray diffraction (XRD; Bruker D8 Advance) and X-ray photoelectron spectroscopy (XPS; Thermo Scientific, K-alpha) with monatomic argon ion beam cleaner. Scanning electron microscopy (SEM) imaging for the morphological analysis was conducted with Jeol JSM-6010. The resistivity measurements were made for MoO_X deposited on the FTO coated substrates under various O_2/Ar ratio following standard procedure.[10,13] The current-voltage characteristics were measured with a potentiostat PARSTAT MC (Princeton Applied Research, AMETEK). The photovoltaic properties were measured under simulated AM1.5 solar irradiation (100 mW cm^{-2}) using a Newport Sol3A Class AAA solar simulator with a 450W xenon short-arc lamp. The measured material parameters were used for the calculation of the energy diagram. Equations for deriving a schematic energy diagram followed a previously reported procedure,[22,25] and can be found in the supplementary material. The dopant density for the GaP wafers is given by the supplier (GaP:S; ~$2 \cdot 10^{18}$ cm^{-3}). To determine the expected tunneling currents between the GaP and MoO_X, electronic tunneling calculations were employed using the Wentzel-Kramers-Brillouin (WKB) approximation,[26] which allows one to determine the tunneling current density.

RESULTS AND DISCUSSION

Optical properties

The MoO_X thin films with a nominal thickness of 150 nm were prepared on FTO glass substrate at various O_2/Ar ratio (6/14, 7/13 and 8/12 sccm) to determine the effect of composition ratio on the optical band-gap of the film. As shown in Fig. 2a, all samples exhibited a high transmittance (> 80% in the visible range), and the band-gap was estimated to be 2.75-2.83 eV according to the Tauc plot (inset) with indirect allowed transition (*i.e.*, n = ½), which is proportional to the oxygen flow ratio. This is a result of the higher ratio of stoichiometric trioxide phases with wide absorption edge, and this trend is in good agreement with that from previous studies.[27,28] Increased transmittance was observed after the post-annealing process in the case of the MoO_X with O_2/Ar ratio of 6/14 sccm, along with a slight increase in band-gap. This might be due to the Burstein–Moss shift[29,30] caused by the Fermi-level shift to higher energy in a heavily doped semiconductor. Generally, non-stoichiometric oxides with excess metal cations due to insufficient oxygen during the deposition results highly doped oxide layer, and the sample with low oxygen ratio (*i.e.*, 6/14 sccm) is in this case.

XRD analysis

The structural properties of MoO_X thin films were characterized in order to analyze the composition and the orientation of the films. The X-ray diffraction is therefore examined, for both the as-deposited and the post-deposition annealed samples. Fig. 2b depicts the diffraction peaks of the MoO_X deposited on FTO glass substrate. As shown with the dashed line, the film seems to keep its amorphous nature for both as-deposited and annealed sample at an annealing temperature of 200˚C. The characteristic peaks related to MoO_X form a rather wide, low intensity, and broad diffraction peak around 30-32˚ in which (204) plane assigned to the hexagonal MoO_3 phase. The distinct reflections at 2θ of 26.3˚ indicate the formation of h-MoO_3 with (210), but, substantial overlap with the characteristic peak from the FTO coated substrate makes it hard to distinguish in the XRD data. Though the peak overlap, the reversed intensity ratio between the 26.3˚ and 37.8˚ implies the existence of the (210) plane for all MoO_X samples. It is worth to note that the peak at 26.3˚ may be derived from the MoO_2 (111), and thus we conducted XPS analysis to investigate the composition of films. Zhang et al. demonstrated that the crystallinity of the MoO_X thin film was observed from the temperature over 150°C.[31] Albeit no significant increase of the intensity or peak width change has not been observed in the present study, an advanced analysis bulk-sensitive technique, such as Raman spectroscopy,[5] is needed in further development.

XPS analysis

The MoO_X thin films were examined using X-ray Photoelectron Spectroscopy (XPS) to obtain quantitative data regarding their chemical states and surface morphology as well as to determine their electronic structure. As

shown in Figure 3a, the valence band of the films can be reduced slightly by thermal post-annealing in ambient N_2 as demonstrated in the stacked spectra. This VB shift towards the Fermi level (E_F) is observed from all samples regardless of the oxygen ratio. The valence band spectra are known to be dominated by the mostly O 2p derived bands, and no noticeable shift upon possible creation of oxygen vacancies during the heat-treatment has been observed indicating that oxygen vacancies are not acting as shallow donors in MoO_X as shown in the previous study.[5]

The sputtered MoO_X films were subsequently exposed to ion-beam to remove the adventitious carbon at the surface. Battaglia et al.[5] demonstrated a negative shift of VB position after a UV-ozone exposure on their evaporated MoO_X films to remove the carbonaceous contamination. Exploration of the cleaned surface is particularly important from a device fabrication viewpoint where the hole transfer layer is deposited in the vacuum forming a MoO_X/GaP interface. Naturally, the samples exposed to ambient conditions may have different oxidation states from the one from the as-deposited. It is evident from survey scans that the untreated samples have distinct peaks that correspond to carbon (C 1s scan) while cleaned samples show a significantly decreased carbon trace (Fig. S2). It is also evidenced by the deconvoluted XPS spectrum (Figure 4) that show significantly reduced peaks from the oxygen with the carbon bond (*i.e.*, C-O and C=O). We emphasize that no significant residue of unexpected elements at the surface has been observed after the cleaning process used for this XPS analysis (Fig. S2). Though MoO_X was formed using a sputtering technique and subsequent ion-beam surface cleaning, it appears that the trend in VB remained the same.

The small defect band visible at a binding energy of around 1.5 eV is also of particular interest. This mid-gap defect state has been observed in other XPS studies on MoO_X films. Though its origin remains a source of controversy, identifying its position is vital for understanding the hole transfer pathway in band alignment of the full device. Its spectral weight suppressed with post-annealing treatment (Figure 3a and b, dotted line) and this decrease may be due to the carbon contamination from the probably not thoroughly cleaned quartz tube. However, surface cleaning by ion-beam shallow etching (2-3 nm) reveals that the center of defect state drifts apart from the E_F. The broad peak within 0.5-2.5 eV can be related to the presence of Mo^{4+} and Mo^{5+} (Figure 4) that contributes to the mid-gap states near 2 eV as observed in previous work by Inzani et al.[27] In this context, the shift of the defect state towards the E_F can be understood by the fact that relatively lower number of oxygen vacancy in MoO_X film formed at high O_2/Ar flow ratio may suppress of Mo^{4+} and Mo^{5+} from the MoO_2 and Mo_2O_5 phases, respectively (Figure 4a and c). XPS depth profiling on the ion-beam cleaned MoO_X prepared at O_2/Ar ratio of 6/14 also confirms (Fig. S3) fairly stable contribution from the deconvoluted peaks and composition ratio throughout the thickness of the material. The extracted values of the valence band and mid-gap center plotted in Figure 3c are also listed in Table 1.

Table 1. XPS binding energy values for the valence band edge and mid-gap center of MoO_X at various conditions.

O_2/Ar ratio	Treatment	VB, eV	Mid-gap center, eV
6/14	No	2.62	1.56
	Ion-beam cleaned	2.64	1.87
7/13	No	2.72	1.46
	Ion-beam cleaned	2.56	1.79
8/12	No	2.69	1.43
	Ion-beam cleaned	2.48	1.65

J-V characteristics

J-V measurements were performed in order to study the electrical conductivity at room temperature of the as-deposited and post-treated MoO_X films under various O_2/Ar ratio on FTO-coated glass followed by Cu (50 nm) and Au (50 nm) deposition to form a current collector. The results from the devices investigated under direct bias between the FTO (positive) and Au (negative) are shown in Fig. 5a. The overall conductivity of the MoO_X is estimated to be about $2\sim4\cdot10^{-6}$ S cm^{-1} from the J-V measurement. The conductivity is calculated from the low bias potential (up to 1 V) in order to compare the conductivity of the whole set of samples; still, it only showed small variations. As explained by Oh et al.,[32] stoichiometric MoO_3 is a transparent and insulating material, whereas MoO_2 is a metal-like conductor. The electrical conductivities of MoO_3 and MoO_2 are reported to be in the range of $10^{-10} \sim 10^{-11}$ S cm^{-1} and $10^5 \sim 10^4$ S cm^{-1}, respectively.[10] Here, the results from both XPS and electrical

studies point out that mixed phase of stoichiometric MoO_3 and substoichiometric MoO_X result in moderate conductivities of the order 10^{-5} S cm^{-1}, which agree with previously published result.[10]

Photoelectrochemical characteristics

The sputtered MoO_X film with an O_2/Ar ratio of 6/14 was selected as an HTL for the GaP-devices since the deep mid-gap state position (*i.e.*, 1.9 eV from the Fermi level) would provide the closest pathway from the valence band of the n-GaP after the equilibrium. Based on band alignment with a shifted Fermi level of the GaP as illustrated in Fig. 5b, the n-GaP/MoO_X structure is expected to provide a better charge transfer than MoO_X with p-GaP case, where the hole can travel along the shallow upward bend-bending within the p-type semiconductor as calculated in the previous study.[33] Similar experimental precedent researches have been reported for the silicon-based solar cell applications. As demonstrated previously, the GaP-based photocathodes have been operated in acidic environments for water splitting under applied bias,[16,25] but not yet studied for the solar-rechargeable RFB application in detail. In the current study, the choice of redox pairs is inspired by recently reported RFBs.[24,34]

As seen from the cyclic voltammograms (CVs) in Fig. 6a, the redox couples appear reversible, and the redox potential is as expected from previous reports.[34,35] The I^-/I_3^- couple is known to exhibit complex redox chemistry due to the tendency for reactants and products to strongly adsorb on electrode surfaces.[34] We note that a continuous nitrogen gas bubbling and stirring have been provided during the CV measurements to minimize any unexpected chemical reactions from the strongly adsorbed species. The catholyte consists of 2 mM AQS with a supporting electrolyte with 0.5M H_2SO_4, and the anolyte contains 2 mM NaI with the same supporting electrolyte condition. The redox potentials were evaluated as the mid-point potential between the anodic and cathodic peaks. Both redox reactions are two-electron transfers with apparent quasi-reversible kinetics as seen from the CVs, and these results bring a cell potential of 0.56 V for the flow cell containing the negative (I_3^-/I^-) and positive ($AQS/AQSH_2$) electrolytes at 50% state-of-charge. The battery performs well, and the time dependence of the voltage shows a Nernstian behaviour. However, while the test with 20 mM AQS catholyte and 60 mM NaI anolyte (upper) shows the continuous decrease of charging/discharging cycle time (*i.e.,* decreasing capacity), cycling test with a mixed catholyte (20 mM AQS + 40 mM NaI) shows quite stable charging/discharging cycle time indicating improved battery capacity (see also charging/discharging capacity behavior in Fig. S4 in supplementary material). The unstable capacity behavior in the single electrolyte case might be ascribed to cross-over which is generally led by osmotic pressure and ionic strength differences between the catholyte and anolyte.[36] Ionic strength (I) calculation (see section 1 in supplementary material) reveals that ionic strengths for the mixed electrolyte case are well-balanced ($I_{catholyte} = I_{anolyte} = 1.56$ mol liter^{-1}), whereas the cell only with 20 mM AQS in 0.5M H_2SO_4 shows low $I_{catholyte}$ of 1.52 mol liter^{-1}. Moreover, the Osmotic pressure in the catholyte side with the mixed electrolyte increased from 78.1 to 87.2 Pa, which is close to the value for the anolyte side (87.8 Pa). Further optimization of electrolyte mixture is out of the work scope, and the primary focus of the present work is on the photo-charging of redox couples with $AQS/AQSH_2$ and I_3^-/I^-; however, it should be addressed in further development, and a detailed investigation is underway.

Figure 6c shows the photocurrent density (J_{ph}) as a function of the applied potential in three-electrode setup for both p-GaP and n-GaP samples coupled with Pt conducting layer and MoO_X HTL deposited under 6/14 O_2/Ar ratio. The data were recorded under 1 sun illumination in 20 mM AQS solution only (*i.e.*, 0% state-of-charge). The photo-induced cathodic current from the Pt/n-GaP/MoO_X architecture has an onset around 0.63 V_{RHE}, while Pt/p-GaP/MoO_X showed a significantly low onset around 0.15 V_{RHE}. Onset potentials will in the following be referred to as $V_{on,light}$ and $V_{on,dark}$ for the photo-illuminated and dark condition, respectively. The J_{ph} also proportionally increases by more than two-fold when n-GaP is used as a photo-absorber. Considering the estimated CB edge of the MoO_X and VB of the GaP, this behaviour implies alternative charge transfer *via* mid-gap states, as illustrated in Fig. 5b giving rise to increased minority carrier flow from the bulk towards the space charge region.

However, as demonstrated in previous studies,[16,25] the photocurrent ranges far behind the performance of p-GaP devices under water-reduction condition (*i.e.*, HER), which showed one order of magnitude higher photocurrent. This poor performance cannot be explained by the electrical conductivity of the MoO_X film since the range is within values reported previously.[10] This may be attributed to the uncontrolled oxidation at the GaP/MoO_X interface, which hinders facile charge transfer across the interface. Considering the fact that the MoO_X

is annealed at 200°C, the GaP surface would be oxidized during the deposition process. The oxidized GaP is known as an electrical insulator which is believed to be an interfacial barrier at the interface.[37]

To improve the charge transfer, the interface between the n-GaP and MoO_X was modified using an interlayer at the interface. The LSV performed using a sample with a Mo interlayer between the GaP and MoO_X (Fig. 6d) showed a significantly increased photocurrent, which is close to 1 mA cm^{-2} level, indicating that hole transfer from the n-GaP was remarkably improved. The LSV curve obtained under dark (dashed line) also reveals that no significant dark current (due to corrosion, for instance) is observed. The comparative study between LSVs (Fig. S5a) from a Pt-coated electrode and the sample with the modified MoO_X indicates that photovoltage is approximately 0.4 V. The onset potential of a simple Pt/GaP device (dashed curve in Fig. S5) also reveals that contribution from the GaP/MoO_X junction to the photovoltage is around 0.3 V. We also observed considerable hysteresis during the CV measurements (Fig. S5 b), particularly for the charged electrolyte. This observation represents clear evidence for mass transport limitations, which could likely be ameliorated with the faster flow, or a modified cell geometry.[34] Actually, the addition of a thin metal layer prior to the oxide deposition has been employed previously by water splitting devices with low-bandgap photocathodes that are readily oxidized.[2,38,39] For instance, a Ti thin layer for the c-Si/TiO_2 interface is shown to protect the c-Si substrate by sacrificial self-oxidation during the following TiO_2 deposition process.[2,7] The Co adlayer deposited onto c-Si before CoO_X and $NiCoO_X$ can be understood in the same context.[39] While the photocurrent shows a significant improvement, a negative shift of the V_{on} takes place compared to the one from the sample without the Mo interlayer. This might be due to remnant Mo or Mo-rich phases which can be a possible recombination site.

Another interesting point is the case with SiO_X interlayer (inset, Fig. 6d). The SiO_X has been broadly applied to PEC devices owing to its outstanding surface passivating property.[7,40] The LSV from a thin SiO_X interlayer (1-2 nm) in inset has a $V_{on,light}$ of 1.19 V which is almost two times higher than the one without any interlayer in Fig. 6c. The difference between the current density obtained under dark operation and the one under light-illumination reveals the J_{ph} of this Pt/n-GaP/SiO_X/MoO_X structure barely reaches 15 µA cm^{-2} (at 0 V_{RHE}), and this unforeseen *J-V* response may be attributed to the poorly controlled thickness of the SiO_X. According to Wentzel–Kramers–Brillouin (WKB) approximation, even 1 nm uncontrolled thickness change can lead to an order of magnitude decrease of tunneling current limit. Here, it is noted that the thickness of the sputtered films was controlled using a traditional linear thickness estimation in terms of deposition time using a QCM monitoring. A problem with this method is the low accuracy. Further optimization of the SiO_X film for maximizing the J_{ph} has not been conducted in the present study; however, it should be addressed in further development.

The photoelectrochemical performance of the full solar flow cell was characterized by LSVs and unbiased photoresponse under two-electrode configuration (inset) shown in Fig. 7. The long-term unbiased photocurrent record (inset) agrees well with the magnitudes of the photocurrents (in the range 0.02 – 0.3 mA) obtained from the intersection of the two curves (*i.e.*, current matching between the photocathode and carbon-rod electrode). An interesting aspect is that the photocurrent increased with the operating time, and then stabilized after the first 12 hours showing the operating current between 0.3 – 0.4 mA (1.5 – 2.0 mA cm^{-2}). Furthermore, the V_{on} of the long-term tested GaP photocathode increased significantly by approximately 150 mV compared to that of the LSV curve taken right before the long-term CA measurement. This unforeseen *J-V* response may be attributed to the enhanced charge transfer mechanism owing to the increased active area resulted from the corrosion of the GaP substrate in an acidic environment. As shown in Fig. 7b, the top-down view of the Pt/GaP/Mo/MoO_X device taken from the edge of the sample represents the morphological effect of the long-term experiment. The unexposed region shows a dense Pt-coated surface without any apparent cracks or damages, while the area exposed to the electrolyte has a porous structure with pores with a diameter of 0.1 – 0.3 µm, indicating that the sputtered thin Pt conducting layer cannot properly prevent the corrosion of the n-GaP in acidic condition. The resultant porous structure displayed a morphology that is similar to the one that was observed previously for GaP-based nanowire structure.[41,42]

As illustrated in Fig. 7b and c, the porous films produced due to the corrosion process of the n-GaP (100) here are known to have a high aspect ratio that pores are formed perpendicular to the surface plane in the direction of the current flow.[41] The high aspect ratio architecture that provides a shortened lateral carrier pathway can decouple the physical constraints from the limited minority carrier diffusion length seen in GaP semiconductors (*e.g.*, ≤ 5 µm for high-quality GaP wafer).[43] The energy-diagrams (Fig. 7d) calculated based on the procedure described elsewhere support that the charge transport for both holes and electrons at both ends. As evidenced

by photo-current output (~0.4 mA cm^{-2} @ 0 V_{RHE}) observed experimentally from the bare n-GaP device (Fig. S6 in supplementary material), it appears reasonable to assume that the increased activity is mainly attributed to the enhanced charge transfer *via* both Pt conducting layer and bare GaP surface as illustrated in Fig. 7e.

However, at the same time, the results in Fig. 7 imply that the stability of the photocathode would not be sufficient to uphold a durable photocurrent. For instance, further chemical damage can form pin-holes leading to direct shunt-paths. Unlike the silicon-based materials, where the self-deactivation by oxidation or silanol group formation takes place,[2,38] the GaP is known to be decomposed at pH below 3 and forms Ga^{3+} and $GaOH^{2+}$. Albeit the improvement of the chemical stability of the GaP substrate is technologically not easy, it is likely that one could avoid the chemical damage via applying a protective layer which screens completely the substrate from the electrolyte as demonstrated elsewhere.[2,39,41,44] Actually, the Pt conducting layer formed onto the n-GaP surface is designed to isolate the substrate from the electrolyte, and at the same time, provide a facile charge transfer. Optimization of Pt coverage over the entire surface is beyond the scope of this paper; however, it must be addressed in further development.

CONCLUSION

The GaP-based device for photo-charging of the redox flow battery has been modified by various hole-transfer-layer (HTL) structures. We have introduced MoO_X as an HTL for the back-illuminated GaP photocathode charging the solar redox flow cell based on anthraquinone and iodide redox couples across the Pt conducting layer and carbon-felt anode. The band structure and energy diagram for the charge transport through the mid-gap states of the MoO_X was characterized *via* XPS with an ion-beam surface cleaning step. The Pt/n-GaP/MoO_X photocathode, especially with Mo interlayer, has shown improved performance in terms of photovoltage and photocurrent. Specifically, the implementation of a GaP/MoO_X junction with Mo interlayer leads to the enhancement of photovoltage by 0.3 V, as evidenced by *J-V* characterizations. It is shown that direct solar charging of an aqueous AQS/I RFB cell is possible without the need for externally applied bias. The results shown in the present work represent an opportunity of using the MoO_X for the GaP-based device as an HTL layer that can expand its use for solar-rechargeable RFB applications. The sole implementation of the MoO_X HTL may prove to be insufficient for driving a redox reaction at meaningful photocurrent, but it could possibly be impactful in combination with an electron transport layer at another side of the device. The remained bottleneck, however, is the poor stability of n-GaP limiting the operating time and state-of-charge consequently. The use of especially protective layer with appropriate surface coverage would offer a significant opportunity for the realization of a stable photo-charging device system as demonstrated in the solar water splitting field.

SUPPLEMENTARY MATERIAL

See the supplementary material for further details on band alignment calculation method, UV-Vis transmittance, XPS survey and depth profile, LSV for n-GaP/MoO_X, Pt/n-GaP, and Pt film, CV using a charged electrolyte, and the charging/discharging measurements with normalized capacity data, and Mott-Schottky analysis on the n-Gap.

CONFLICTS OF INTEREST

There are no conflicts to declare.

AUTHOR CONTRIBUTIONS

[‡]These authors contributed equally. D.B. designed the experiments, prepared the manuscript, performed XRD and XPS analysis and co-supervised G.K. with W.A.S. G.K. performed the device fabrication and measurements of the PEC behaviors. K.W. provided electrochemical analysis on redox couples and E.D. prepared AQS used for the redox reactions and performed redox flow battery operation with D.B under co-supervision by A.B and W.A.S. The manuscript was written through contributions of all authors. All authors have approved the final version of the manuscript.

ACKNOWLEDGEMENTS

This work was supported by the LEaDing Fellowship grant from the European Union's Horizon 2020 research and Innovation Programme under the Marie Sklodowska-Curie grant agreement no. 707404. D.B. also acknowledges Erasmus+ staff mobility for training grant from the European Commissions for financial support during the

research stay at Aarhus University. The authors also thank Dr. D. N. Østedgaard-Munck at Aarhus University for assistance in operating the redox flow, and Joost Middelkoop and Herman Schreuders at the MECS group of TU Delft for preparation of the PEC flow cell and assistance with the vacuum deposition system. The authors also acknowledge B. Norder and Bart Boshuizen at the department of chemical engineering of TU Delft for XRD and XPS training, respectively. D.B. thanks Dr. Mauro Malizia at the University of Cambridge for guidance with the GaP wafer selection.

REFERENCES

[1] H. Kawasaki, K. Konishi, D. Adachi, H. Uzu, T. Irie, K. Yoshikawa, K. Nakano, T. Uto, W. Yoshida, K. Yamamoto, and M. Kanematsu, Nat. Energy **2**, 17032 (2017).

[2] D. Bae, B. Seger, O. Hansen, P.C.K. Vesborg, and I. Chorkendorff, ChemElectroChem **6**, 106 (2019).

[3] X. Li, F. Xie, S. Zhang, J. Hou, and W.C.H. Choy, Light Sci. Appl. **4**, 1 (2015).

[4] F. Wang, S. Zhao, B. Liu, Y. Li, Q. Ren, R. Du, N. Wang, C. Wei, X. Chen, G. Wang, B. Yan, Y. Zhao, and X. Zhang, Nano Energy **39**, 437 (2017).

[5] C. Battaglia, X. Yin, M. Zheng, I.D. Sharp, T. Chen, S. McDonnell, A. Azcatl, C. Carraro, B. Ma, R. Maboudian, R.M. Wallace, and A. Javey, Nano Lett. **14**, 967 (2014).

[6] J. Bullock, D. Yan, A. Cuevas, Y. Wan, and C. Samundsett, Energy Procedia **77**, 446 (2015).

[7] D. Bae, T. Pedersen, B. Seger, B. Iandolo, O. Hansen, P.C.K. Vesborg, and I. Chorkendorff, Catal. Today **290**, 59 (2017).

[8] S. De Wolf, A. Descoeudres, Z.C. Holman, and C. Ballif, Green **2**, 7 (2012).

[9] F. Li, Y. Zhou, M. Liu, G. Dong, and F. Liu, ArXiv (2019).

[10] J. Bullock, A. Cuevas, T. Allen, and C. Battaglia, Appl. Phys. Lett. **105**, (2014).

[11] O. Almora, L.G. Gerling, C. Voz, R. Alcubilla, J. Puigdollers, and G. Garcia-Belmonte, Sol. Energy Mater. Sol. Cells **168**, 221 (2017).

[12] B. Mei, A. a Permyakova, R. Frydendal, D. Bae, T. Pedersen, P. Malacrida, O. Hansen, I.E.L. Stephens, P.C.K. Vesborg, B. Seger, and I. Chorkendorff, J. Phys. Chem. Lett. **5**, 3456 (2014).

[13] J. Tong, Y. Wan, J. Cui, S. Lim, N. Song, and A. Lennon, Appl. Surf. Sci. **423**, 139 (2017).

[14] Z.S. Bittner, D. V. Forbes, M. Nesnidal, and S.M. Hubbard, Conf. Rec. IEEE Photovolt. Spec. Conf. 001959 (2011).

[15] S. Hu, M.R. Shaner, J. a Beardslee, M. Lichterman, B.S. Brunschwig, and N.S. Lewis, Science **344**, 1005 (2014).

[16] A. Standing, S. Assali, L. Gao, M.A. Verheijen, D. van Dam, Y. Cui, P.H.L. Notten, J.E.M. Haverkort, and E.P.A.M. Bakkers, Nat. Commun. **6**, 7824 (2015).

[17] W. Li, H.C. Fu, Y. Zhao, J.H. He, and S. Jin, Chem **4**, 2644 (2018).

[18] S. Liao, X. Zong, B. Seger, T. Pedersen, T. Yao, C. Ding, J. Shi, J. Chen, and C. Li, Nat. Commun. **7**, 11474 (2016).

[19] Q. Cheng, W. Fan, Y. He, P. Ma, S. Vanka, S. Fan, Z. Mi, and D. Wang, Adv. Mater. **29**, 1 (2017).

[20] K. Wedege, D. Bae, E. Dražević, A. Mendes, P.C.K. Vesborg, and A. Bentien, RSC Adv. **8**, 6331 (2018).

[21] M. Ah Sen, Molybdenum Oxide Thin Films for Heterojunction Crystalline Silicon Solar Cells, Delft University of Technology, 2017.

[22] D. Bae, G.M. Faasse, G. Kanellos, and W.A. Smith, Sustain. Energy Fuels **3**, 2399 (2019).

[23] D. Bae, B. Seger, M. Malizia, I. Chorkendorff, P.C.K. Vesborg, T. Pedersen, O. Hansen, and A. Kuznetsov, Energy Environ. Sci. **8**, 650 (2015).

[24] K. Wedege, E. Dražević, D. Konya, and A. Bentien, Sci. Rep. **6**, (2016).

[25] M. Malizia, B. Seger, I. Chorkendorff, and P.C.K. Vesborg, J. Mater. Chem. A **2**, 6847 (2014).

[26] S. Krishnamoorthy, D.N. Nath, F. Akyol, P.S. Park, M. Esposto, and S. Rajan, Appl. Phys. Lett. **97**, 1 (2010).

[27] K. Inzani, M. Nematollahi, F. Vullum-Bruer, T. Grande, T.W. Reenaas, and S.M. Selbach, Phys. Chem. Chem. Phys. **19**, 9232 (2017).

[28] S. Erfanifam, S.M. Mohseni, L. Jamilpanah, M. Mohammadbeigi, P. Sangpour, S.A. Hosseini, and A. Iraji Zad, Mater. Des. **122**, 220 (2017).

[29] E. Burstein, Phys. Rev. **93**, 632 (1954).

[30] H. Search, C. Journals, A. Contact, M. Iopscience, and I.P. Address, **775**, (1954).

[31] C. Liu, Z. Li, and Z. Zhang, Sci. Technol. Adv. Mater. **14**, (2013).

[32] M. Sook Oh, B. Seob Yang, J. Ho Lee, S. Ha Oh, U. Soo Lee, Y. Jang Kim, H. Joon Kim, and M. Soo Huh, J. Vac. Sci. Technol. A Vacuum, Surfaces, Film. **30**, 031501 (2012).

[33] W. Yoon, J.E. Moore, E. Cho, D. Scheiman, N.A. Kotulak, E. Cleveland, Y.W. Ok, P.P. Jenkins, A. Rohatgi, and R.J. Walters, Jpn. J. Appl. Phys. **56**, (2017).

[34] J.R. McKone, F.J. DiSalvo, and H.D. Abruña, J. Mater. Chem. A **5**, 5362 (2017).

[35] M. Quan, D. Sanchez, M.F. Wasylkiw, and D.K. Smith, J. Am. Chem. Soc. **129**, 12847 (2007).

[36] Z. Xu, I. Michos, X. Wang, R. Yang, X. Gu, and J. Dong, Chem. Commun. **50**, 2416 (2014).

[37] S.M. Spitzer, B. Schwartz, and M. Kuhn, J. Electrochem. Soc. **120**, 669 (1973).

[38] D. Bae, B. Seger, P.C.K. Vesborg, O. Hansen, and I. Chorkendorff, Chem. Soc. Rev. **46**, 1933 (2017).

[39] D. Bae, B. Mei, R. Frydendal, T. Pedersen, B. Seger, O. Hansen, P.C.K. Vesborg, and I. Chorkendorff, ChemElectroChem **3**, 1546 (2016).

[40] M.J. Choi, J.-Y. Jung, M.-J. Park, J.-W. Song, J.-H. Lee, and J.H. Bang, J. Mater. Chem. A **2**, 2928 (2014).

[41] S. Lee, A.R. Bielinski, E. Fahrenkrug, N.P. Dasgupta, and S. Maldonado, ACS Appl. Mater. Interfaces **8**, 16178 (2016).

[42] M. Treideris, I. Simkiene, A. Selskis, Z. Balevicius, and G.J. Babonas, Acta Phys. Pol. A **119**, 131 (2011).

[43] T. Tiedje, E. Yablonovitch, G.D. Cody, and B.G. Brooks, IEEE Trans. Electron Devices **31**, 711 (1984).

[44] D. Bae, S. Shayestehaminzadeh, E.B. Thorsteinsson, T. Pedersen, O. Hansen, B. Seger, P.C.K. Vesborg, S. Ólafsson, and I. Chorkendorff, Sol. Energy Mater. Sol. Cells **144**, 758 (2016).

Figure 1. Schematic cross section with approximate band alignment of the sample before equilibrium (a) and structure with thickness information of the device used in this study (b). The schematic illustration of PEC flow cell with 2-electrode configuration is also shown (c). Depending on the fabrication condition, some samples have a MoO_X/GaP interface with an interlayer (*e.g.*, SiO_X or Mo). Note that all illustrations are not to scale.

Figure 2. (a) UV-Vis transmittance spectra of MoO_X deposited with various O_2/Ar gas flow ratio on a FTO-coated glass substrate. The signal from the quartz substrate was subtracted as a background spectrum. Tauc plot converted from the transmittance to estimate its band gap also shown as an inset along with optical photo of the samples. Note that the signal from the glass substrate was subtracted as a background spectrum. (b) XRD patterns of MoO_X grown at room temperature and post-annealed at 200˚C (with N_2 flow) are plotted with spectra from the FTO coated glass.

Figure 3. X-ray photoelectron valence band (VB) spectra (a) of the MoO_X film prepared by sputter deposition under various O_2/Ar mixture ratio. Spectra from the post-annealed sample and the one with surface cleaning treatment are plotted with dotted and dot-dash line, respectively. Zoomed-in in of the relevant region for the mid-gap states in the VB is also shown in (b). Extracted VB and mid-gap center values from the annealed and cleaned samples are plotted in (c).

Figure 4. XPS spectra of the Mo 3d and O 1s from the samples with various deposition and post-treatment conditions (O_2/Ar ratio of 6/14 - (a, b); 7/13 and 8/12 – (c, d)) are shown with the deconvoluted peak assignments.

Figure 5. *J-V* curves (in dark) of the MoO_X devices as a function of the O_2/Ar ratio (6/14 – black; 7/13 – blue; 8/12 –red) (a) and schematic band alignment at an interface between the MoO_X and p- and n-GaP substrates are illustrated (b). The inset shows the extracted conductivities from the *J-V* curve using Ohm's law. The device schematic used to measure the dark J-V is also illustrated (upper left). The detail calculation procedure for the energy diagram for the (b) can be found in the section 2 in supplementary material.

Figure 6. CVs of 2 mM solutions of AQS (black) and NaI (blue) in 0.5M H_2SO_4 supporting electrolyte (a) using a scan rate of 10 mV sec^{-1}. (b) Charge/discharge curves in a 25 cm^2 commercial RFB cell with a constant current density of 1.1 mA cm^2 for the single-compound electrolyte (upper) and mixed-electrolyte cases (lower). (c) shows the LSV curves in 20 mM AQS (in 0.5M H_2SO_4 supporting electrolyte) for both n-GaP and p-GaP PEC devices with MoO_X HTL and Pt conducting layer. LSV curves under the same condition, but using samples with interlayer (1-2 nm of SiO_X or Mo) are demonstrated in (d).

Figure 7. LSVs of back-illuminated GaP photocathode with the MoO_X HTL and Pt conducting layer (black) and carbon anode (dark blue) in a three-electrode cell (a). The solid and dashed curves correspond to the LSV measured before and after the long-term (46.7 hours) chronoamperometry (CA) measurement in two-electrode setup (inset). SEM image of the sample surface (top-down view) after the long-term experiment can be found in (b) with its cross-sectional view in (c). Note that the upper and lower images correspond to the electrolyte exposed area and non-damaged with thick Pt film (green), respectively. (d) demonstrates the schematic band diagram of the device tested in the Fig. 7a. The calculation procedure can be found in the supplementary material (section 2) of this work. (e) illustrates how the photo-excited charges are separated and transferred to the electrolyte through the roughened structure.

1

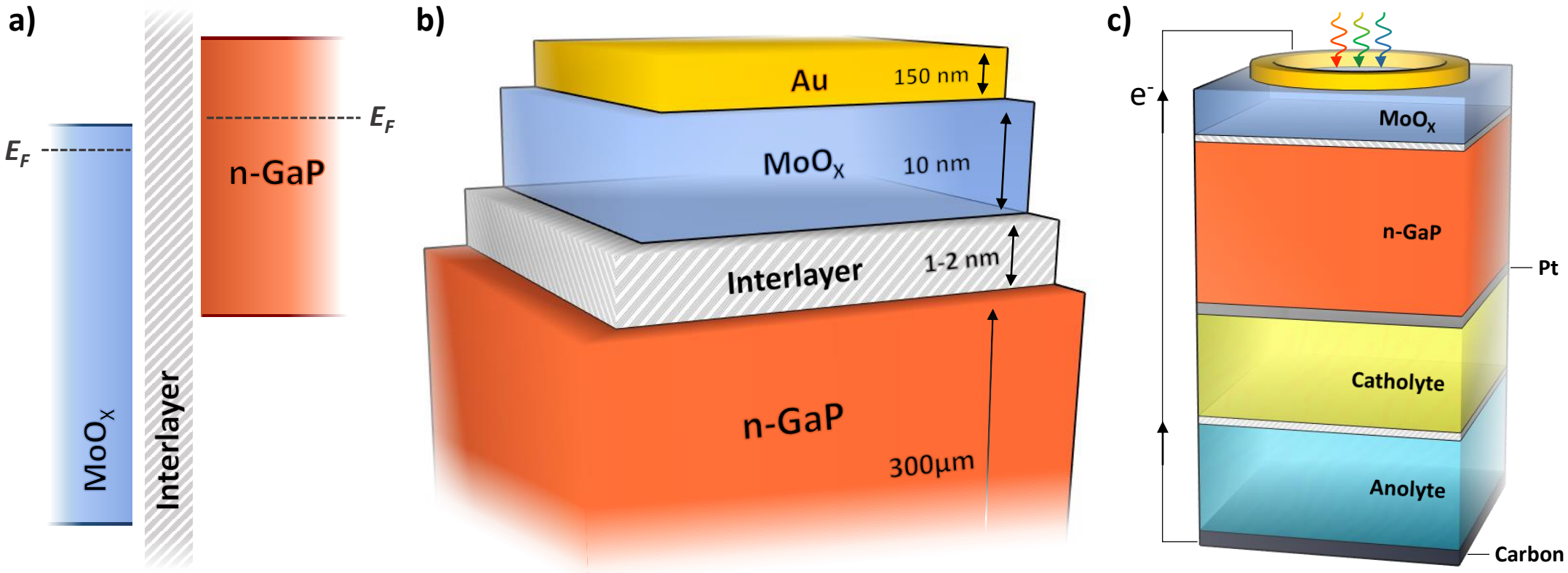
a)
E_F
E_F
n-GaP
MoO_X
Interlayer
b)
Au
150 nm
MoO_X
10 nm
Interlayer
1-2 nm
n-GaP
300µm
c)
e⁻
MoO_X
n-GaP
Pt
Catholyte
Anolyte
Carbon

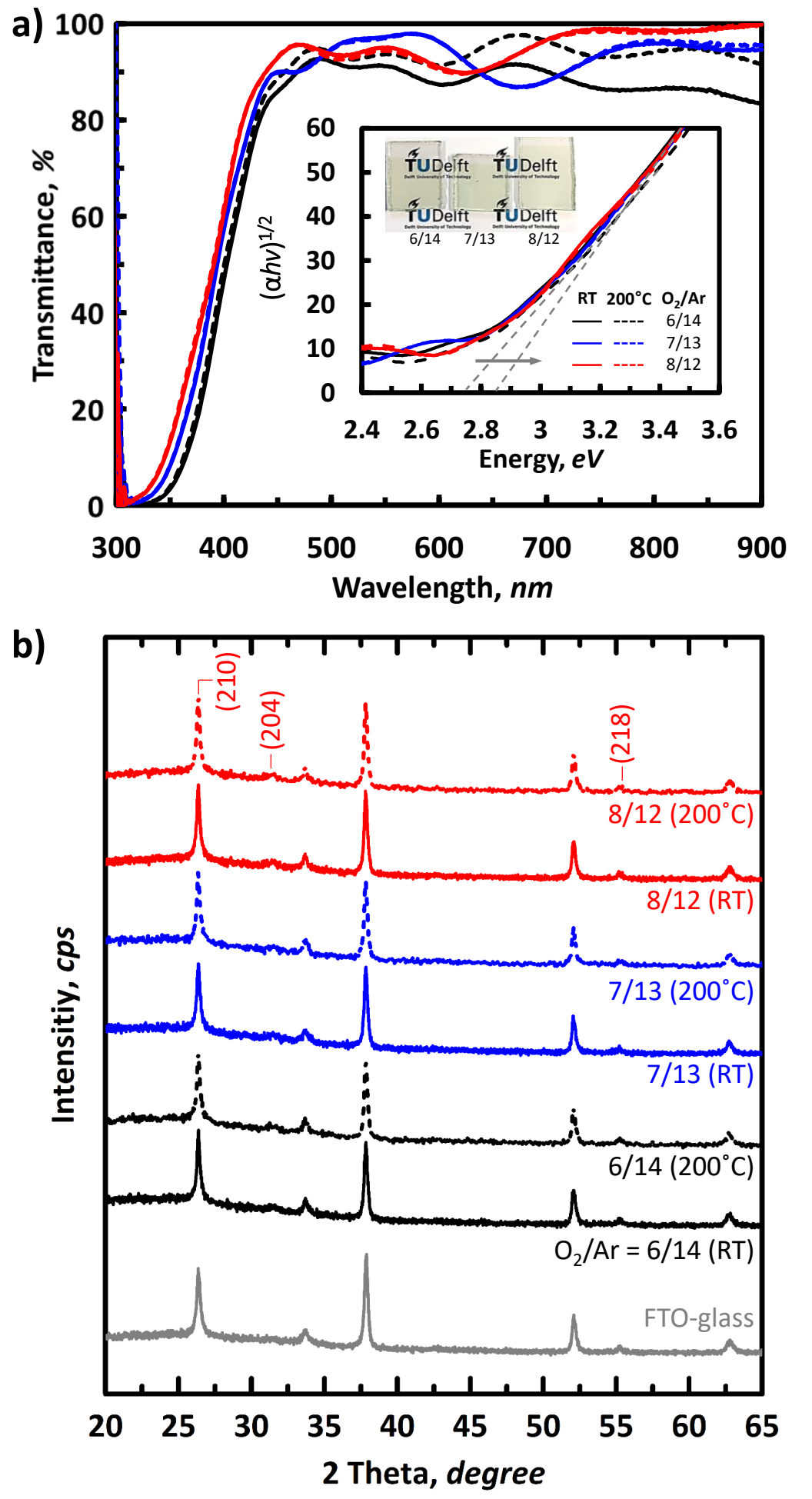
a)
Transmittance, %
Wavelength, nm
(αhν)^1/2
Energy, eV
RT 200°C O2/Ar
6/14
7/13
8/12
b)
Intensitiy, cps
2 Theta, degree
(210)
(204)
(218)
8/12 (200˚C)
8/12 (RT)
7/13 (200˚C)
7/13 (RT)
6/14 (200˚C)
O2/Ar = 6/14 (RT)
FTO-glass

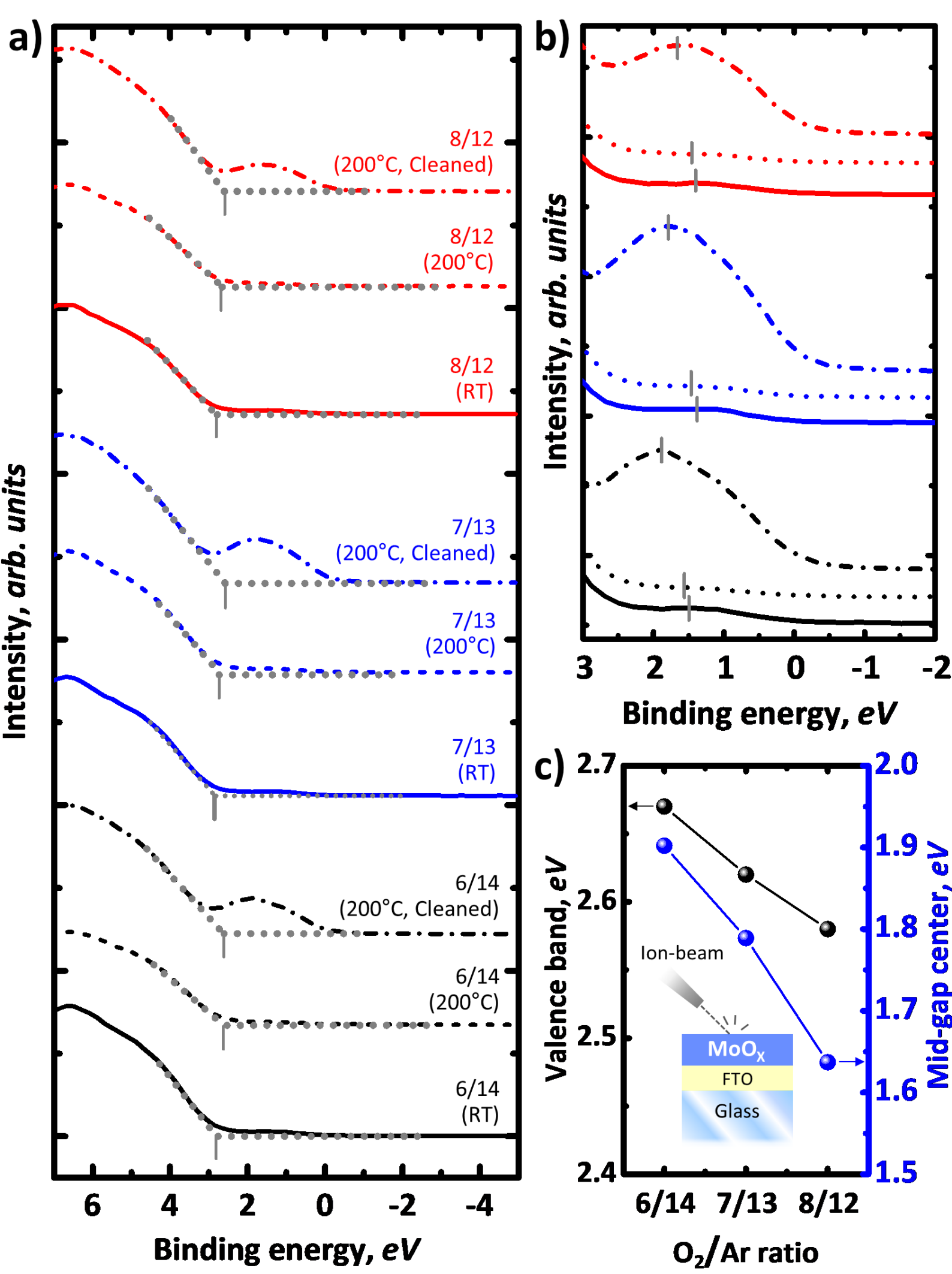
a)
8/12
(200°C, Cleaned)
8/12
(200°C)
8/12
(RT)
7/13
(200°C, Cleaned)
7/13
(200°C)
7/13
(RT)
6/14
(200°C, Cleaned)
6/14
(200°C)
6/14
(RT)
Intensity, arb. units
6
4
2
0
-2
-4
Binding energy, eV
b)
Intensity, arb. units
3
2
1
0
-1
-2
Binding energy, eV
c)
Valence band, eV
2.7
2.6
2.5
2.4
Mid-gap center, eV
2.0
1.9
1.8
1.7
1.6
1.5
Ion-beam
MoOx
FTO
Glass
6/14
7/13
8/12
O2/Ar ratio

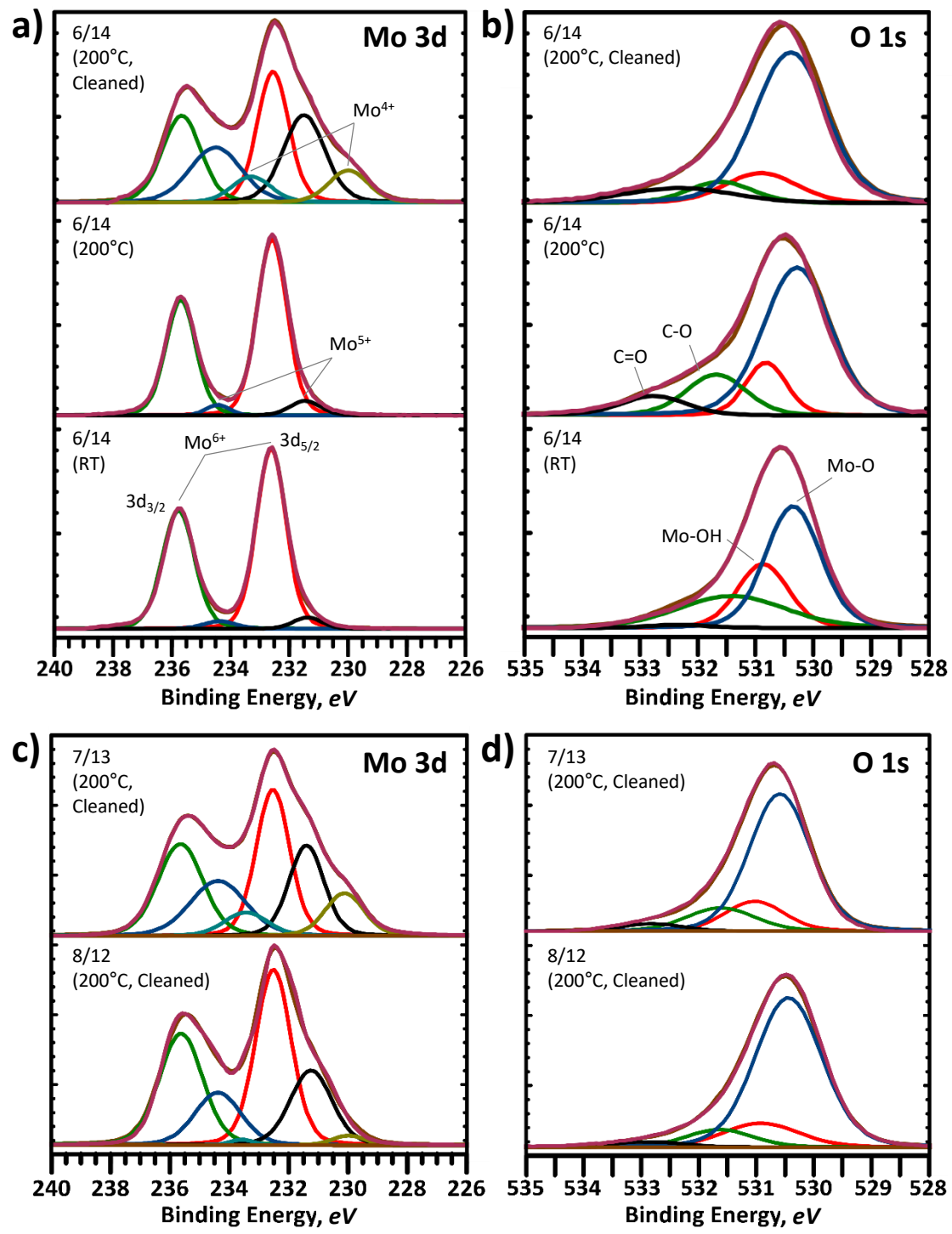
a)
Mo 3d
6/14
(200°C,
Cleaned)
Mo4+
6/14
(200°C)
Mo5+
6/14
(RT)
Mo6+
3d5/2
3d3/2
240 238 236 234 232 230 228 226
Binding Energy, eV
b)
O 1s
6/14
(200°C, Cleaned)
6/14
(200°C)
C=O
C-O
6/14
(RT)
Mo-O
Mo-OH
535 534 533 532 531 530 529 528
Binding Energy, eV
c)
Mo 3d
7/13
(200°C,
Cleaned)
8/12
(200°C, Cleaned)
240 238 236 234 232 230 228 226
Binding Energy, eV
d)
O 1s
7/13
(200°C, Cleaned)
8/12
(200°C, Cleaned)
535 534 533 532 531 530 529 528
Binding Energy, eV

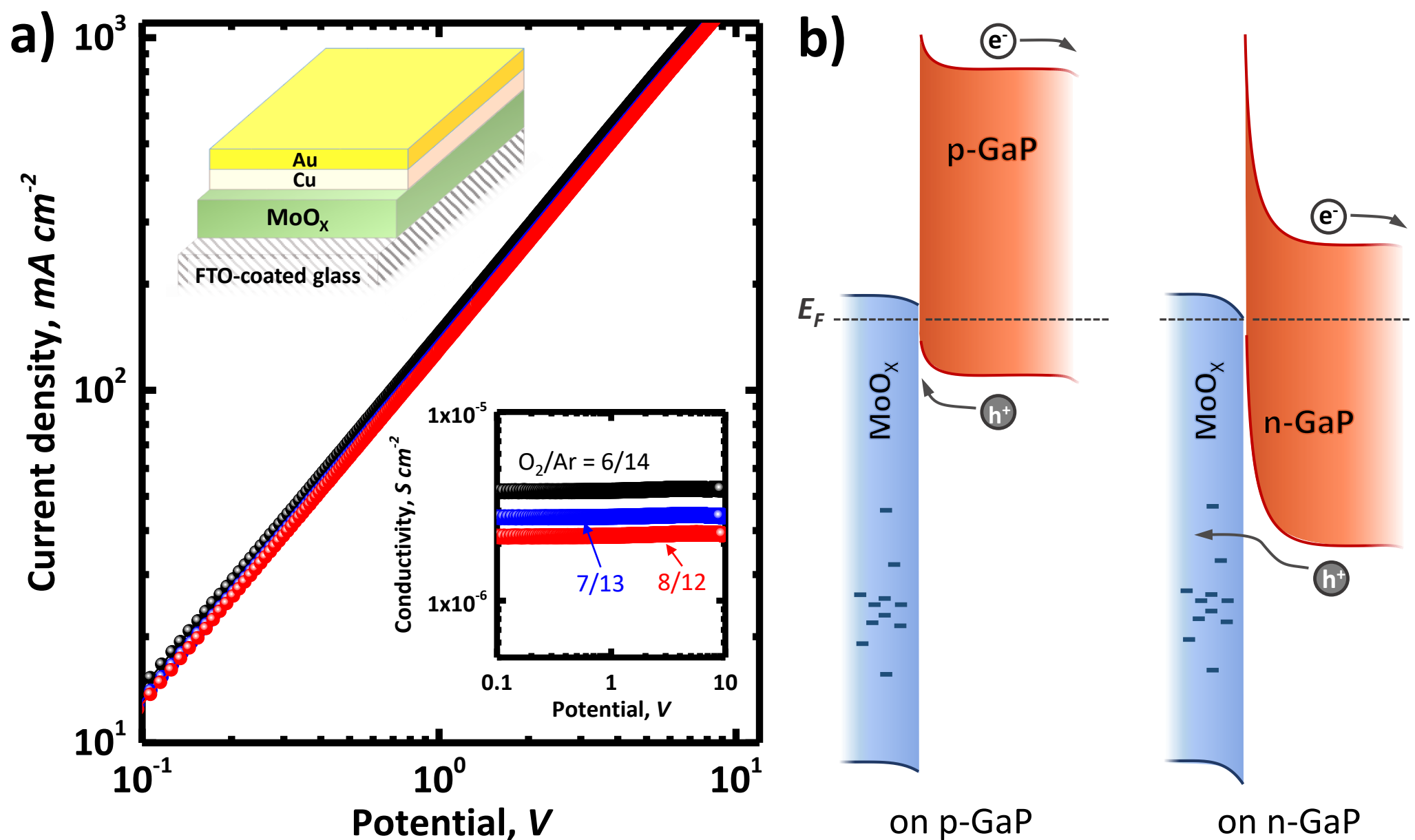
a)
Current density, mA cm-2
Potential, V
Au
Cu
MoOX
FTO-coated glass
Conductivity, S cm-2
O2/Ar = 6/14
7/13
8/12
Potential, V
b)
e-
p-GaP
EF
MoOX
h+
n-GaP
on p-GaP
on n-GaP

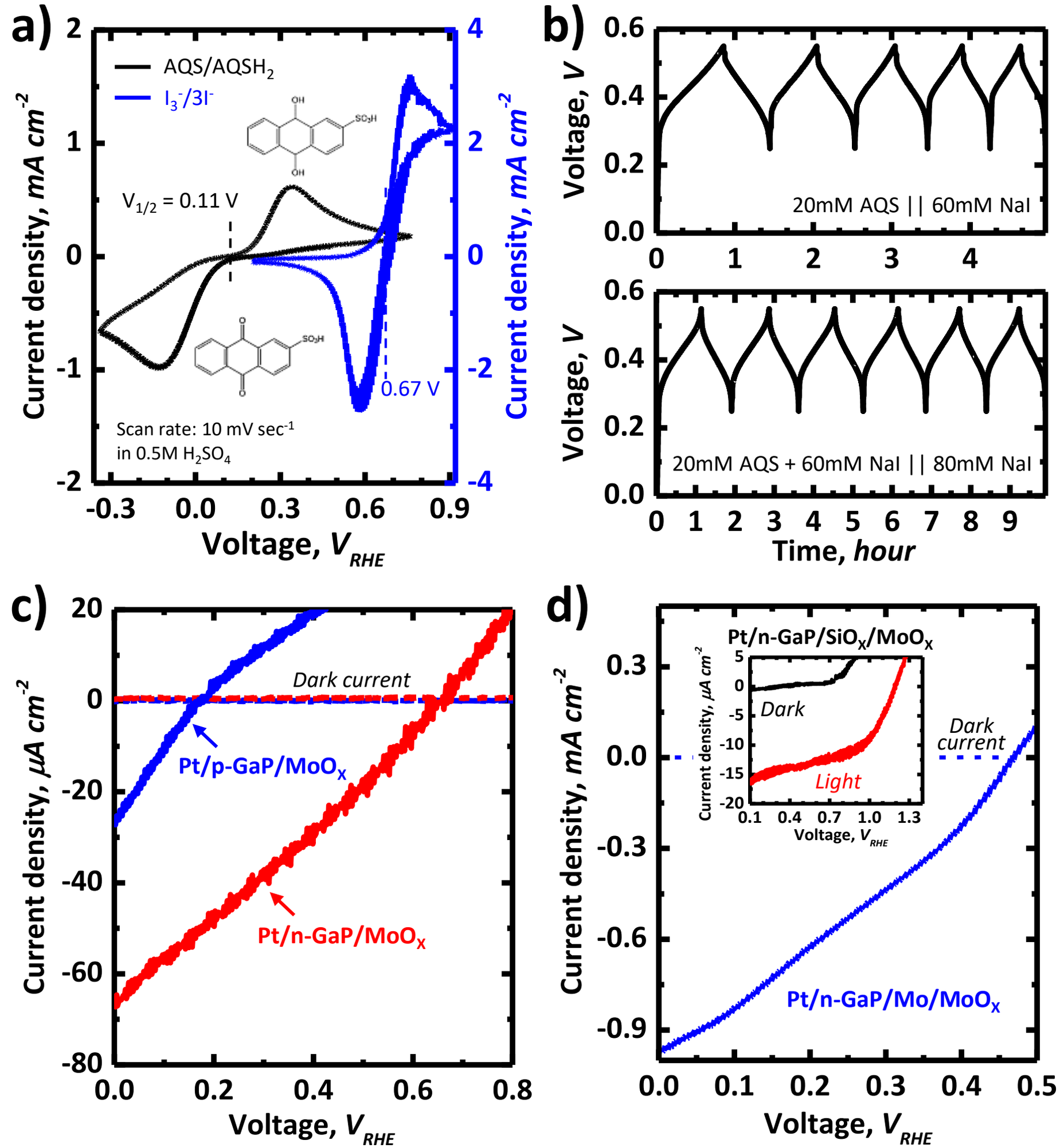
a)
AQS/AQSH2
I3-/3I-
V1/2 = 0.11 V
0.67 V
Scan rate: 10 mV sec-1
in 0.5M H2SO4
Current density, mA cm-2
Current density, mA cm-2
Voltage, VRHE
b)
20mM AQS || 60mM NaI
20mM AQS + 60mM NaI || 80mM NaI
Voltage, V
Time, hour
c)
Dark current
Pt/p-GaP/MoOX
Pt/n-GaP/MoOX
Current density, μA cm-2
Voltage, VRHE
d)
Pt/n-GaP/SiOX/MoOX
Dark
Light
Dark current
Pt/n-GaP/Mo/MoOX
Current density, mA cm-2
Current density, μA cm-2
Voltage, VRHE

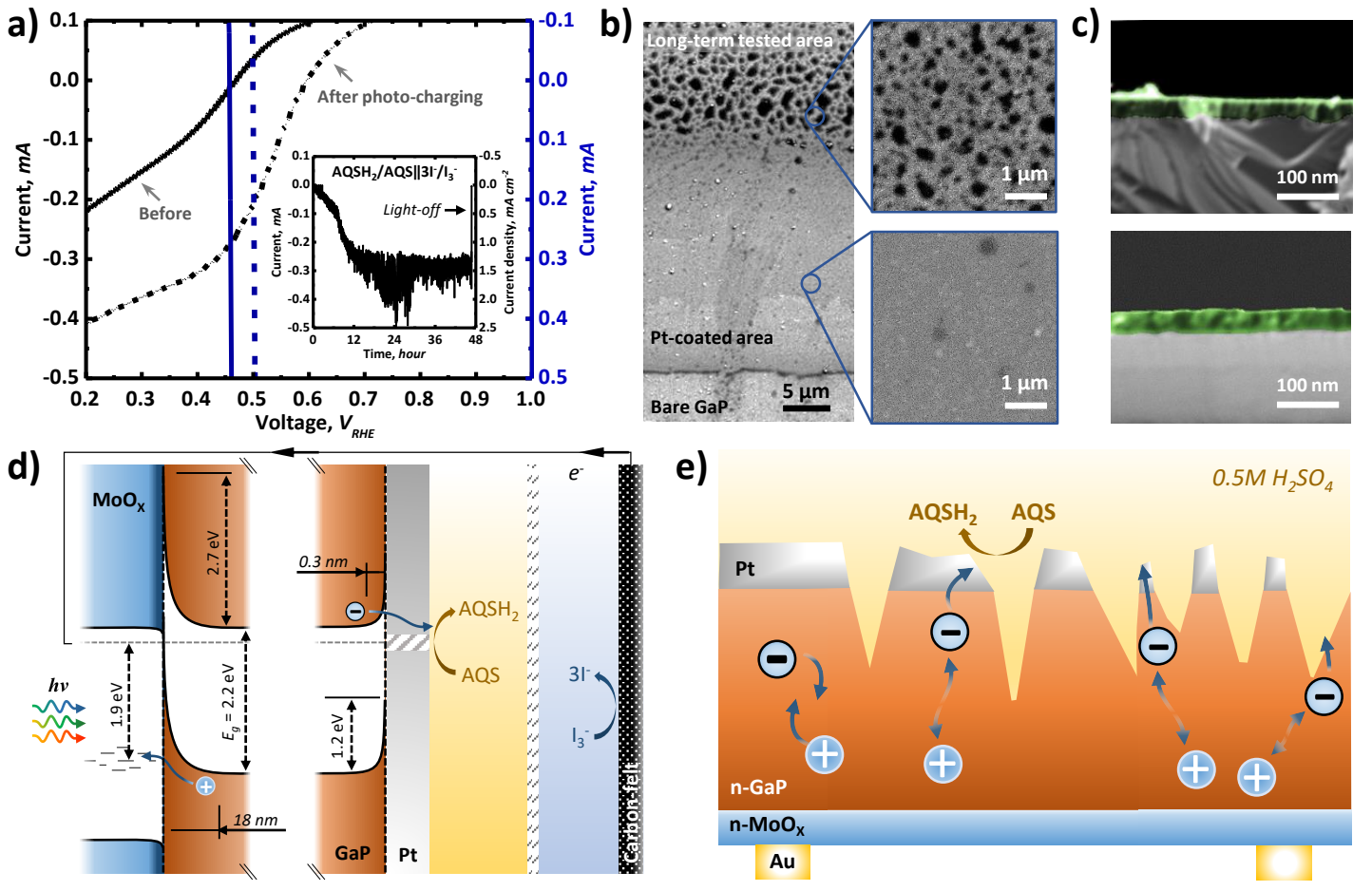
a)
Current, mA
Voltage, V_{RHE}
Before
After photo-charging
AQSH2/AQS||3I-/I3-
Light-off
Current, mA
Current density, mA cm-2
Time, hour
b)
Long-term tested area
1 µm
Pt-coated area
5 µm
Bare GaP
1 µm
c)
100 nm
100 nm
d)
MoOx
2.7 eV
0.3 nm
AQSH2
AQS
e-
3I-
I3-
hv
1.9 eV
Eg = 2.2 eV
1.2 eV
18 nm
GaP
Pt
carbon-felt
e)
0.5M H2SO4
AQSH2
AQS
Pt
n-GaP
n-MoOx
Au